

Supporting Information

Climbing the volcano of electrocatalytic activity while avoiding catalyst corrosion: Ni₃P, a hydrogen evolution electrocatalyst stable in both acid and alkali

Anders B. Laursen^a, Robert B. Wexler^b, Marianna J. Whitaker^a, Edward J. Izett^a, Karin U.D. Calvino^a, Shinjae Hwang^a, Ross Rucker^c, Hao Wang^a, Jing Li^a, Eric Garfunkel^a, Martha Greenblatt^{a,*}, Andrew M. Rappe^{b,*}, and G. Charles Dismukes^{a,d*}.

AUTHOR ADDRESS: ^a Department of Chemistry and Chemical Biology at Rutgers, The State University of New Jersey, 610 Taylor Road, Piscataway NJ 08854, USA, ^b Department of Chemistry, University of Pennsylvania, 231 S. 34 Street, Philadelphia, PA 19104-6323, USA. ^c Department of Materials Science and Engineering at Rutgers, The State University of New Jersey, 607 Taylor Road, Piscataway NJ 08854, USA ^d Waksman Institute of Microbiology, Rutgers, The State University of New Jersey, 190 Frelinghuysen Road, Piscataway, NJ 08854, USA.

* dismukes@chem.rutgers.edu; rappe@sas.upenn.edu; martha@chem.rutgers.edu.

Experimental procedures:

Catalyst synthesis: 1.5 mol% stoichiometric excess of P(s,red) (Alfa-Aesar 99%) and stoichiometric amounts of Ni(s) (Sigma-Aldrich < 150µm) were thoroughly mixed in a mortar. The powder was transferred to a quartz tube that were evacuated and sealed after cleaning with Ar by back-filling 2-3 times. The evacuated tubes was placed in a furnace, heated to 700°C, and kept there for 24 hr. Heating rates were modest to facilitate a slow reaction between the Ni(s) and P(s,red). This avoids excessive local heating due to the exothermic reaction. Temperatures were ramped as follows: (1) 80°C to 250°C over 580 min with a 360 min dwell time, (2) 250°C to 350°C over 300 min with a 200 min dwell time, (3) 350°C to 450°C over 300 min with a 200 min dwell time, and (4) 450°C to 700°C over 350 min with a 24 h dwell time. Samples were then allowed to cool to room temperature. Sample purity was checked by PXRD and additional Ni(s) or P(s,red) was added if necessary, following the instructions above. In this case, heating was accelerated, *i.e.* temperatures were ramped from 80°C to 700°C over 580 min with a 24 h dwell time. This allows a faster reaction without risking local hotspots due to the low amount of Ni(s) and P(s,red) precursors.

Electrode fabrication: 100 mg of catalyst powder was suspended in 250 µL of 5% Nafion previously neutralized with NaOH. The suspension was mixed by mortar and pestle until dry and fully dried under vacuum for several hours. 50 mg of the resulting catalyst/polymer composite was pressed with a force of 5 tons in a 6 mm diameter die or an equivalent pressure of 17.3 N/mm². The resulting pellet was cut in half, and each half was mounted on a Ti plate (Sigma-Aldrich) using a drop of Ag-paint (SPI supplies). Prior to mounting the pellet, the Ti plate was fixed to a Cu wire using Ag-paint. The Cu wire assembly was threaded through a glass tube. After drying, the Ag-paint, the sides of the catalyst pellet, and the Ti plate were isolated from solution by covering in Hysol 1C epoxy (Loctite) all the way up onto the glass tube. The geometric surface area was determined by imaging and measuring the exposed surface using the ImageJ software.

Electrochemical measurements: All solutions were prepared using Millipore water. Electrochemical cells were cleaned using piranha solution, *i.e.* a 1:3 ratio of 35% H₂O₂ and concentrated H₂SO₄, followed by thorough rinsing with Millipore water. A three-electrode setup, with a Selemion membrane or porous glass frit separating the working and counter compartments, was used for all the electrochemical measurements. To avoid the possibility of Pt contamination during stability measurements, a B-doped diamond electrode was used as a counter electrode. A Ag/AgCl (saturated KCl) reference electrode from BAShi (or home-made Hg/HgSO₄/0.5 M H₂SO₄ reference electrode) was used and calibrated to the RHE scale against a freshly cleaned Pt electrode at open circuit potential prior to each measurement. CP data were manually corrected for the uncompensated iR-drop using impedance spectroscopy to determine the uncompensated solution resistance; typical corrections are on the order of < 10 Ω .

To obtain reliable measurements of the Pt standard, the HER activity of a Pt foil was recorded as linear sweeps from reducing to positive potentials to minimize contamination issues. Between sweeps, the electrode was electropolished (several cycles at 100 mV/s from -1.08-0.3 V vs. RHE). Linear sweep voltammetric scan rates were set to 100 mV/s to avoid mass transport limitations.

The experimental determination of limiting potential is complicated by the absence of a rigorous definition of “catalysis onset potential”. To estimate the limiting potential value for Ni₅P₄ MPs, we used the current density achieved at the limiting potential (as determined by DFT calculations) for Ni₃P MPs. As there is no definition of a limiting current, the value obtained for similarly prepared solid-state catalysts and using the same electrode fabrication process should ensure a fair estimate of the limiting potential. Using a geometrical current density of -3.38 mA/cm² yielded an estimated limiting potential of -0.018 mV vs. RHE for Ni₅P₄ MPs.

Characterization: PXRD patterns were recorded on a Bruker AX8 diffractometer. Patterns were fit to standard patterns from the International Crystal Structure Database (ICSD) in the interval of 2 θ [10-70°]. The patterns were fitted using the Rietveld refinement and the final fit goodness was $X^2 = 1.12$ for Ni₃P and 1.54 for Ni₅P₄ respectively. The difference function shows only contributions from the fitted peaks. This indicates that the difference function is mainly due to an insufficient fit of the exact line shape likely due to a large size distribution.

HR-SEM was collected on a ZEIS SEM fitted using emission currents of 5 keV and the in-lens detector. The 10 μ m scale bar was included for reference. Images were recorded without coating the particles with a conductive film. The catalyst powder was dispersed on adhesive carbon tape directly on the aluminum stub, and excess was removed by lightly tapping the stub with a spatula.

ICP-OES was used to detect Ni leaching into the electrolyte after 16 h of continued electrolysis at -10 mA/cm². Samples were taken at specified time intervals and diluted with HNO₃ to yield at least 10% in acid. An added reference of Y (1 ppm) was used to check the sample quality prior to quantification.

SEM-EDS was performed on a Phenom benchtop SEM. Acceleration voltage was 10keV and samples were deposited on adhesive C-tape on Al-stubs. EDS was recorded at 132 μ m sample distance on 13 randomly selected spots. Resulting composition was averaged over all spots.

XPS - see section describing experimental details and results.

Computational Methodology: DFT^{1,2} calculations were carried out using the Quantum Espresso code³. Optimized norm-conserving⁴, designed⁵ pseudopotentials were constructed using the OPIUM code⁶ for both Ni and P to soften their valence electron wavefunctions and ionic potentials. Wavefunctions were expanded in a plane-wave basis with a cutoff energy of 50 Ry. The exchange correlation energy was calculated using Perdew, Burke, and Ernzerhof's form of the generalized gradient approximation (GGA)⁷. Van der Waals interactions were treated using Grimme's semi-empirical DFT-D2 method^{8,9}. This shifts H binding energies by 0.1 eV, thus making it important for the study of the HER, which requires only small overpotentials. Geometry relaxations were performed on all structures with a total force threshold of 1×10^{-3} Ry/au, whereas the convergence threshold for self-consistency was set to 1×10^{-6} Ry/unit cell (8 formula units). A dipole correction was applied in order to remove the artificial electrical field interactions between images¹⁰; this, however, induced a negligible change in the total energy.

Bulk calculations for Ni(fcc), Ni₃P, and Ni₅P₂ were performed to identify the Ni chemical potential ranges where each phase is stable. The Brillouin zone is sampled using *k*-point meshes of 10x10x10, 4x4x8, and 6x6x4 offset from Γ . Experimental and computed bulk lattice constants can be found in the supporting information Table S5. Tighter energy and force thresholds of 1×10^{-8} Ry and 1×10^{-6} Ry/au were used in bulk relaxations of the lattice constants and ionic positions. Calculation of Löwdin charges was performed at a tighter self-consistent field convergence threshold of 1×10^{-10} Ry/unit cell. The surface energy of symmetric slab models for Ni₃P(0001) converges with nine atomic layers and 25 Å of vacuum space. *k*-point grids for the surface slabs were reduced to 4x4x1 also offset from Γ . Detailed explanation of bulk and surface thermodynamic stability can be found in the SI.

The electron localization function was calculated for Ni₃P to determine the nature of its chemical bonding, e.g. metallic, ionic, and covalent.¹¹ Bader charge analysis was performed on both the bulk and surface charge density using the code developed by Henkelman and co-workers.^{12–15}

Preference of Ni₃P for the (001) facet as determined from DFT calculations:

Experimental evidence suggests that Ni₃P (isostructural with Schreibersite, a (Fe/Ni)₃P mineral formed in meteorites) cleaves perfectly along the (001) facet and imperfectly along (010) and (110) (which is expected for less energetically preferred or stable facets).¹⁶ To incorporate the extrapolation of the Schreibersite preference for forming (001) surfaces to the synthetic Ni₃P, we investigated the thermodynamic stability of each facet by performing first-principles, DFT surface energy calculations. For each facet, we generated symmetric slab models whose surface energies are reported in Table S1 and plotted in Fig. S1A.

Table S1: DFT calculated surface energy [J/m²] of the three experimentally observed Schreibersite facets as a function of the chemical potential of Ni ($\Delta\mu_{\text{Ni}}$) (eV).

$\Delta\mu_{\text{Ni}}$	(001)	(010)	(110)	Description
0.00	2.45	2.41	2.84	Bulk phase boundary between Ni ₃ P and Ni

-0.10	2.36	2.41	2.84	Ni-rich
-0.20	2.28	2.41	2.84	Less Ni-rich
-0.34	2.17	2.41	2.84	Bulk phase boundary between Ni ₃ P and Ni ₅ P ₂

Fig. S1A shows that the surface energies of the (010) and (110) facets are independent of the chemical potential of Ni. This is because the bulk terminations of these facets have the same stoichiometry as the bulk. In contrast, the surface energy of the (001) facet depends on $\Delta\mu_{\text{Ni}}$ because its most stable bulk termination, which has a composition of Ni₄P₄, is P-enriched compared to the bulk.

(001) is the most stable facet across most of the region where Ni₃P is stable. There is a small region at very Ni-rich conditions ($\Delta\mu_{\text{Ni}} > -0.04$ eV) where both the (001) and (010) facets are equally favored. These mixed facets would likely only be prevalent under synthesis conditions that would favor a minor Ni₃P formation in a Ni matrix, unlike the synthesis conditions used in this work which only show a minor Ni impurity.

Additionally, as is shown in the main text, the surface reconstruction Ni₃P(s)/Ni₄P₄(001)+V_{Ni}+P, that best explains the observed activity and the results of poisoning experiments, is stable from -0.27 eV < $\Delta\mu_{\text{Ni}}$ < -0.20 eV. Since, the synthesis/electrolysis conditions are clearly in this chemical potential region then it stands to reason that the facet formation should also be evaluated in this region. Figure S1A shows that in the relevant stability region the (001) facet of Ni₃P is dominant.

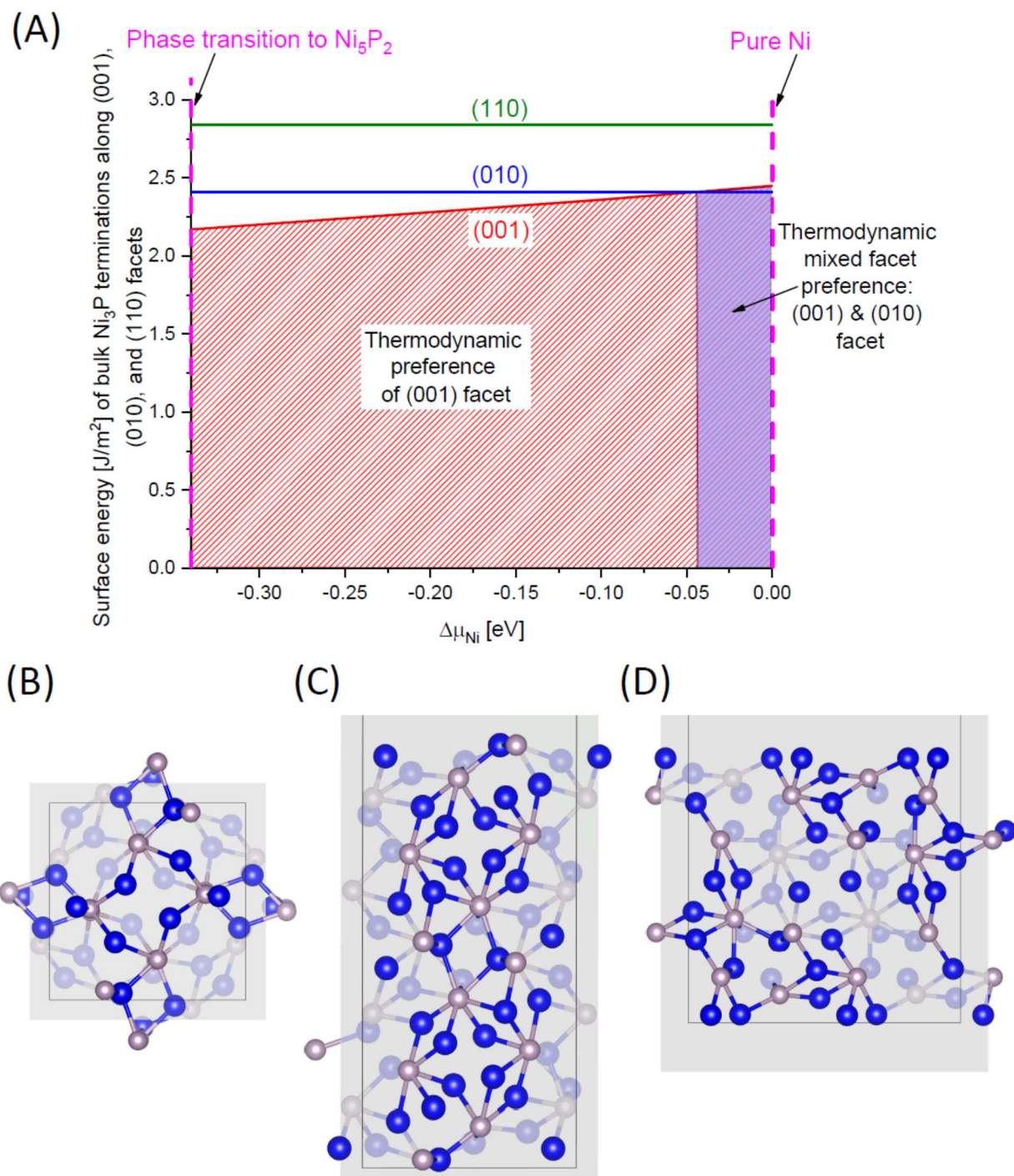


Figure S1 A) DFT calculated surface energy [J/m²] of the (001), (010), and (110) facets as a function of the chemical potential of Ni ($\Delta\mu_{\text{Ni}}$). Surface structure for the investigated facets (Ni in blue and P in purple and translucent gray layer indicates surface/subsurface divide for B) (001), C) (010), and D) (110) facets, respectively.

We further note that the activity of Ni₃P toward the HER depends strongly on the surface P content, with P-rich surfaces being more catalytically active.^{17,18} Therefore, the (010) and (110) facets, whose surfaces possess the same Ni-rich stoichiometry of the bulk, are unlikely to provide facile hydrogen evolution.

HER catalyst performance literature review:

Table S2: Comparison metrics of HER activity for several state of the art electrocatalysts.

Catalyst	Tafel Slope [mV/dec]	j_0 [A/cm ²]	η_{10} [mV]	pH	Citation
Ni ₃ P MP	41±2	$3\pm 1\cdot 10^{-4}$	66	0	This work
Ni ₅ P ₄ MP	30	$5.8\cdot 10^{-4}$	43	0	This work
Ni ₅ P ₄ nc-MP	33	$2.1\cdot 10^{-3}$	33	-0.5	10.1039/C4EE02940B
Ni ₁₂ P ₅	63	$2\cdot 10^{-4}$ *	107	0	10.1021/nn5022204
Ni ₂ P NP	46	$3.3\cdot 10^{-5}$	109	0	10.1021/ja403440e
NiP ₂	51	$2.6\cdot 10^{-4}$ *	75	0	10.1039/C4NR04866K
Pt	30	$2.5\cdot 10^{-3}$	23	0	10.1021/nn5048553, 10.1021/ja403440e
FeP	37	$4.3\cdot 10^{-4}$ *	48	0	10.1021/nn5048553
CoP NP	50	$1.4\cdot 10^{-4}$	74	0	10.1002/anie.201402646
MoS _x thinfilm	40	$1.3\cdot 10^{-7}$ *	202	-0.5	10.1039/c1sc00117e
Exf. MoS ₂	43	$4.2\cdot 10^{-7}$ *	187	0	10.1021/ja404523s
MoS ₂ /rGO	41	$2.5\cdot 10^{-5}$ *	154	0	10.1021/ja201269b
MoS ₂ nanoplate	58	$2.2\cdot 10^{-7}$	380*	0	10.1126/science.1141483
NiMoN _x /C	35.9	$2.4\cdot 10^{-4}$ *	295*	0	10.1002/anie.201200699
NiMo Alloy	132	$7.9\cdot 10^{-5}$	288	14	10.1016/S0013-4686(00)00549-1
NiMo NP	N/A	N/A	82	14	10.1021/cs300691m
Ni ₃ P MP	119±2	$5.2\pm 0.9\cdot 10^{-5}$	291	14	NA
Ni ₅ P ₄ MP	-	-	193	14	NA
Ni ₅ P ₄ nc-MP	98	$4.2\cdot 10^{-3}$	49	14	10.1039/C4EE02940B
Pt	120	$6.9\cdot 10^{-4}$	155*	13	10.1149/1.3483106
Pt	98	$4.0\cdot 10^{-4}$	163	14	This work

The figure below is a heat map similar to Figure 3 in the main manuscript depicting the reported performance for state of the art renewable catalysts (above) in 1M NaOH.

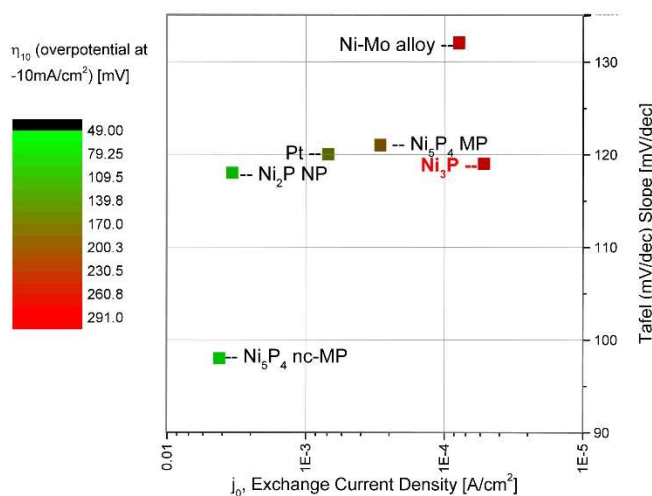


Figure S2 Heat map comparison of performance metrics of state of the art HER electrocatalysts in alkaline electrolyte.

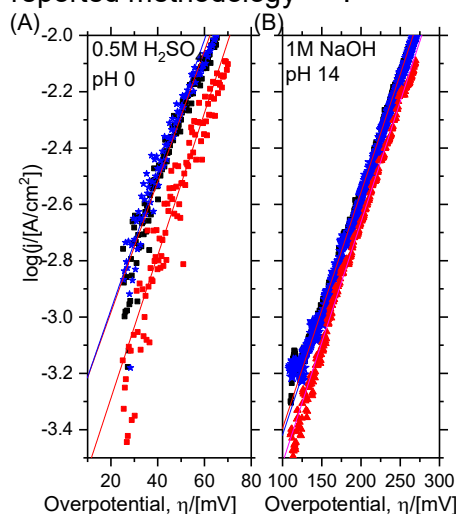
Tafel analysis:

Tafel analysis are performed in triplicates and the standard deviation (sample) for the average of the triplicates is reported. To reduce the contribution from capacitive charging of the porous electrode surface, the individual replicate is averaged over two potential cycles at a low scan rate of 1mV/s. This reduces the capacitive contribution especially at low overpotentials that would otherwise interfere with the Tafel analysis.

Samples are analyzed after the 16hr CP analysis to ensure stationary conditions. Samples are scanned at 1mV/s in either 0.5M H₂SO₄ or 1M NaOH under continuous H₂ bubbling using a B-doped diamond counter electrode, thus avoiding any possible noble metal contamination.

The electrolyte is stirred just below the electrode to minimize the influence of bubbles but linear behavior (Tafel behavior) is still only observed for ~1 decade of current.

Tafel analysis is performed at potentials higher than $\eta = 0.5 \cdot \text{Tafel slope}$ which is the condition satisfying the requirement of the reverse reaction being negligible, in accordance with previously reported methodology^{18,19}.



(C)

Catalyst	pH	Tafel /[mV/dec]	j_0 /[A/cm ²]
Ni ₃ P	0	43.1	$3.57 \cdot 10^{-4}$
		39.5	$1.61 \cdot 10^{-4}$
		41.7	$3.53 \cdot 10^{-4}$
Average		41±2	$3 \pm 1 \cdot 10^{-4}$
Ni ₃ P	14	120.0	$5.51 \cdot 10^{-5}$
		116.9	$4.23 \cdot 10^{-5}$
		119.3	$5.85 \cdot 10^{-5}$
Average		119±2	$5.2 \pm 0.9 \cdot 10^{-5}$

Figure S3 Tafel slope analysis for Ni₃P MPs on three different replicas, including standard deviation between these. (A) in 0.5M H₂SO₄, pH 0 and (B) in 1M NaOH, pH14. (C) table summarizing Tafel analysis results.

For platinum foils the mass transport limitations were significant below -50mV vs RHE and the Tafel analysis thus deviates slightly from what is expected for Pt in the reported literature. Specifically, we obtained a Tafel slope of 35.1mV/dec (in acid) and 97.5mV/dec (in base) the corresponding values in literature are ~30mV/dec and 75mV/dec (albeit at pH13)²⁰. These deviations may be attributable to the practical difficulty in removing H₂ bubbles efficiently from the Pt foil at larger current densities compared to the RDE experiments mostly reported in literature. Exchange current densities were also affected yielding $1.33 \cdot 10^{-4}$ A/cm² in acid and $4.02 \cdot 10^{-4}$ in alkali. Literature reports are around $2.5 \cdot 10^{-3}$ A/cm² (in acid)^{18,21} and $1-6.9 \cdot 10^{-4}$ A/cm² in alkali^{18,20}.

Electrochemical experiments without Nafion binder:

At alkaline pH, Nafion is used in the electrode fabrication primarily as a binder. However, since the Nafion has an internal volume with a high negative charge, the formation of H_2 in alkali could be significantly impeded by the coulombic repulsion between the hydroxide ions formed from water during the HER and the sulfonic acid groups of the polymer. To investigate the extent of this effect, we make electrodes of Ni_3P and Ni_5P_4 MP catalysts without Nafion as a binder, Figure S4 below show the CP analysis of these electrodes.

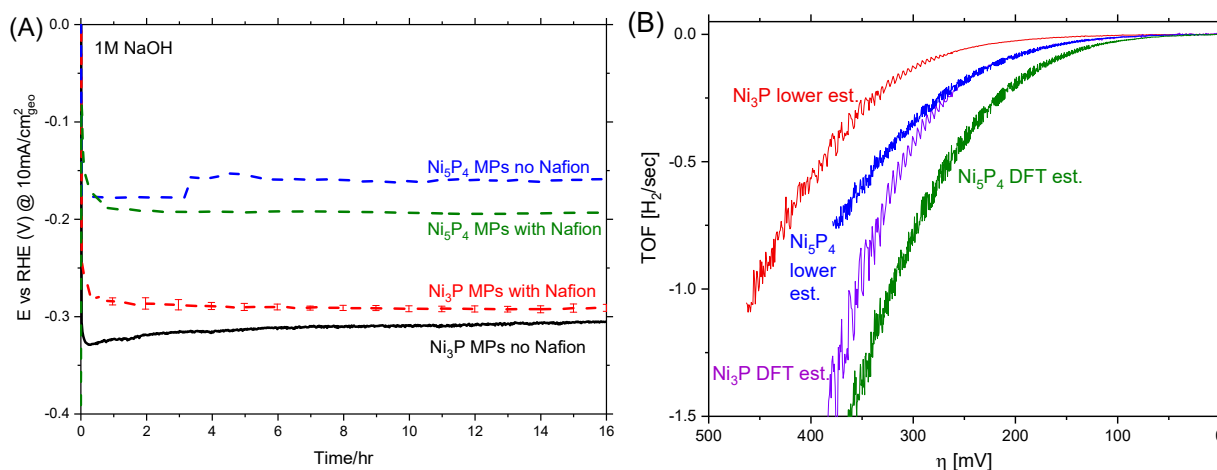


Figure S4 (A) CP analysis at $-10 \text{ mA/cm}^2_{\text{geo}}$ for 16 hours on Ni_3P and Ni_5P_4 MP catalyst electrodes without the Nafion binder in 1M NaOH (pH=0). (B) TOF versus overpotential in 1M NaOH for the Ni_3P MP catalyst using the geometric upper estimate (red) and the DFT based upper estimate (magenta). Ni_5P_4 MP catalyst using the geometric upper estimate (blue) and the DFT based upper estimate (green). Potentials are corrected for solution resistance drop.

The potential required to drive $-10 \text{ mA/cm}^2_{\text{geo}}$ is only changed slightly for either catalyst upon removal of the Nafion binder. The resulting TOF for the Ni_3P MP catalyst is 0.001 s^{-1} with Nafion and 0.004 s^{-1} without Nafion for the Ni_5P_4 MP catalyst the TOF is 0.05 s^{-1} with Nafion and 0.01 s^{-1} without Nafion. The variation in TOF is clearly not correlating with the use of Nafion binder and demonstrates the inherent uncertainty in estimating the TOF for powder electrocatalysts; which clearly can range up to five-fold.

Inductively Coupled Plasma – Optical Emission Spectroscopy — Ni dissolution:

Ni dissolution is tested at the onset of CP measurements and after ~ 16 h up to 48 h of catalysis for Ni_3P in acid. For comparison is given the Ni dissolution for the Ni_5P_4 MP catalyst in acid from 16 h to 24 h of catalysis. The behavior is similar to what we reported for Ni_5P_4 ncMP catalysts,¹⁸ i.e. that the Ni concentration rises initially in acid as the surface nickel phosphate dissolves. Following this

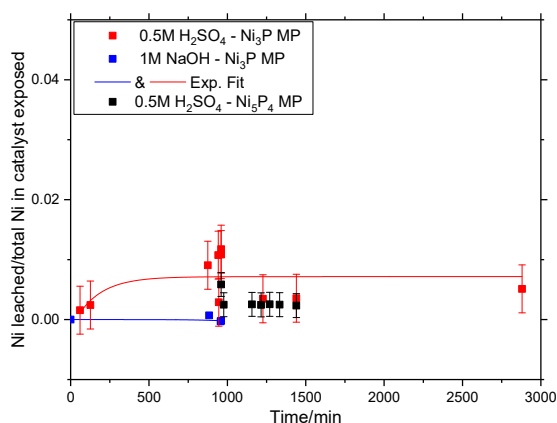


Figure S5 Fraction of Ni entering solution out of total amount exposed in the Ni_3P MP catalyst during HER in 0.5M H_2SO_4 (red) and 1M NaOH (blue), respectively. In addition is shown Ni dissolution from the benchmark catalyst Ni_5P_4 MP in 0.5M H_2SO_4 (black).

increase the Ni concentration levels off as the surface layer is removed and no additional Ni leaches during HER catalysis conditions.

In alkali, no Ni dissolution is observed at all in the first 16 h of catalysis and hence the experiment is not taking to further time points.

The total amount of Ni_3P exposed to the electrolyte is estimated by taking a 2D projection of the surface through the pellet, that is the geometric surface area multiplying with the pellet thickness. The amount of catalyst mass in this volume is expected to potentially interact with the electrolyte. This procedure is similar to that reported in our previous study.¹⁸

The limit of detection ($\text{LOD}_{\alpha=0.05}$) is determined from the 90% confidence interval for the linear regression of the calibration line. The lower limit of the intercept (when plotting concentration vs. OES intensity [a.u.]) corresponds to the LOD.

Platinum dissolution during reference electrode calibration:

Pt concentration was measured in the reaction cell after measurement of the reference potential by ICP-OES. The resultant Pt concentration was <0.0 ppm with an estimated $\text{LOD}_{\alpha=0.05}$ for Pt down to 0.2 ppm.

SEM-EDS:

SEM EDS analysis confirmed the full removal of the Ni impurity detected in the as-

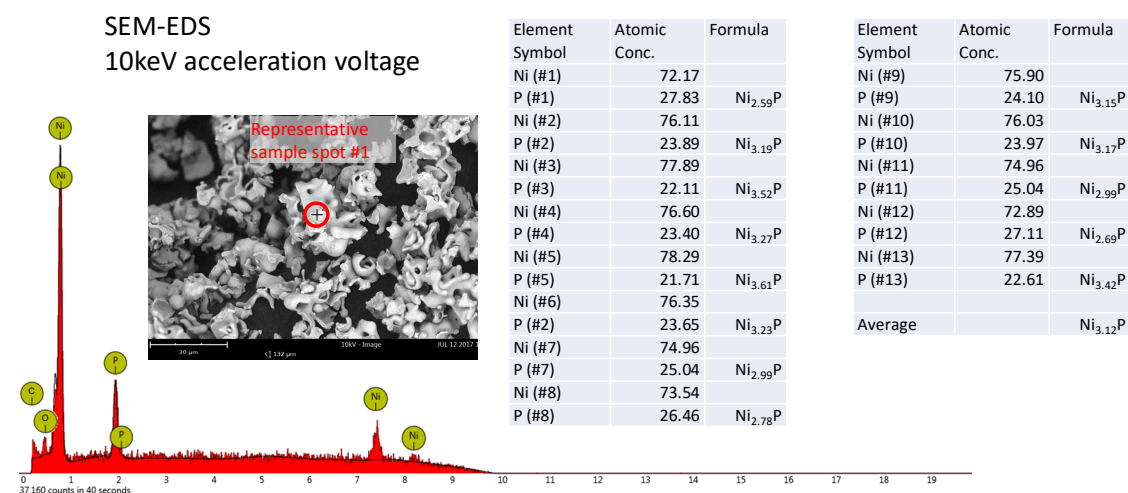


Figure S6 SEM EDS analysis of the pristine Ni_3P MP catalyst.

synthesized Ni_3P MP sample. The final catalyst had the composition: $\text{Ni}_{3.12}\text{P}$ as determined over 13 random samples after the acid washing step. Figure S6 shows a representative spot analysis of Spot#1 and SEM image (image insert) (using backscatter detector) showing the spot position. The table insert shows the atomic concentration of Ni and P in the 13 detected spots and the corresponding empirical formulas.

SEM and PXRD characterization:

PXRD and SEM of Ni_3P and Ni_5P_4 MPs are shown below. From the PXRD both phases can be seen to be phase pure and from SEM to be of approximate the same particle size.

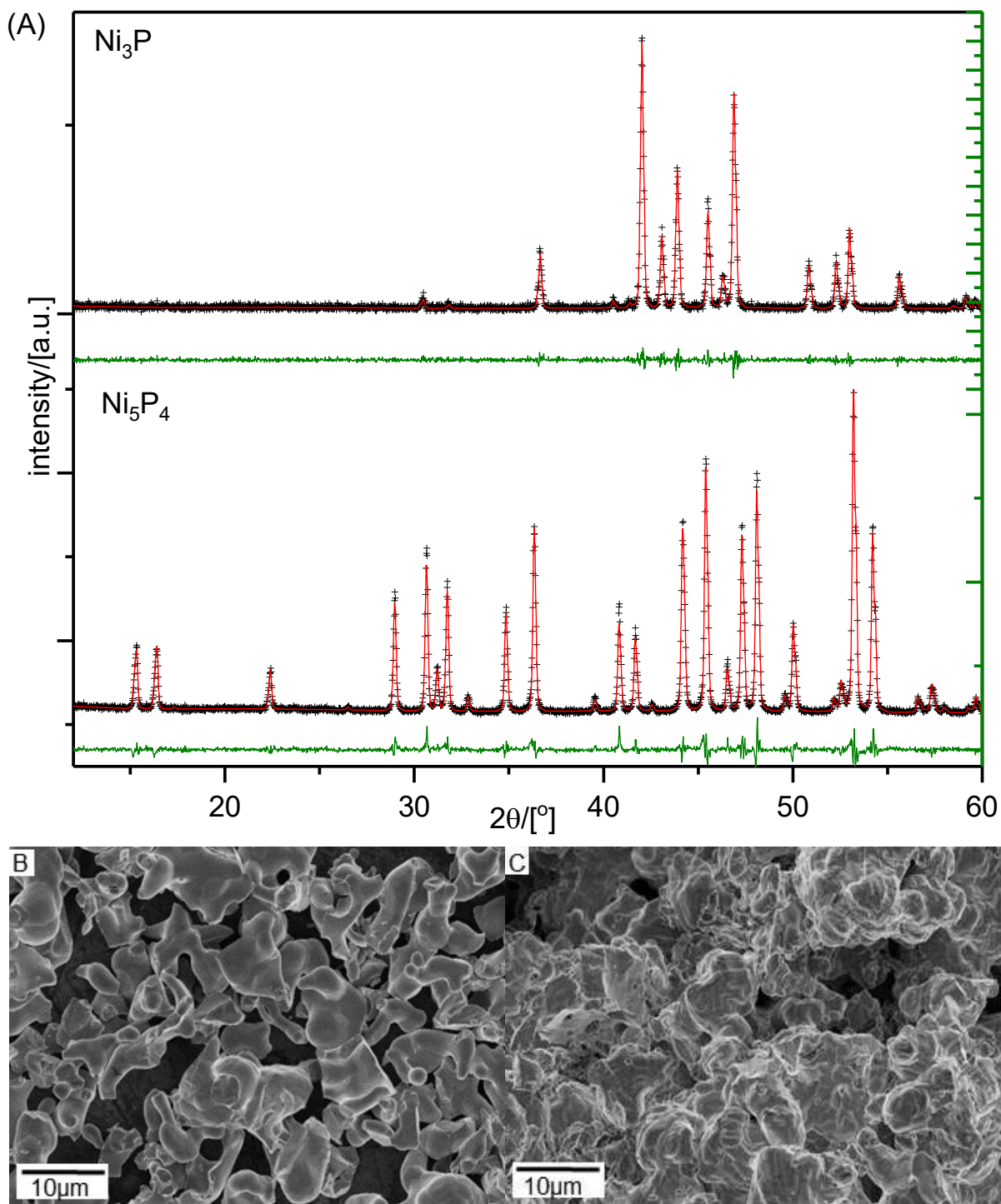


Figure S7 (A) PXRD pattern (**black**), fit (**red**), and residuals (**green**) for Ni_3P and Ni_5P_4 . The final goodness of the fit are: $\chi^2 = 1.15 \pm 0.03$ and 1.65 ± 0.11 for Ni_3P and Ni_5P_4 , respectively. (B) Ni_3P and (C) Ni_5P_4 microparticles synthesized using our solid-state method. Ni_3P and Ni_5P_4 particles have similar sizes but different morphologies.

Turn-over frequency, TOF:

Here we shall calculate HER TOFs for comparison to electrodes made from various procedures. The first method relies on ECSA estimation at the first reductive potential achieving near zero Faradaic current contribution. The catalyst is cycled in the region of -0.1V to 0V vs RHE, this window keeps the catalyst biased at a reductive potential compared to H₂ and is expected to prevent oxidation of the catalyst ensuring the determination of a surface area consistent with that under *in operando* HER conditions. The procedure mirrors that described by Kibsgaard et al. except a negative shift of the potential window²². Once the actual surface area has been estimated a subsequent estimate of average number of sites per surface area relates the current directly to TOF.

The second estimate takes into account that the number of H-surface sites may be different from the average number of surface atoms. For instance for Pt(111) a H site density of $1.5 \cdot 10^{15}$ sites/cm² has been determined whereas the method above estimates the same density as $4.1 \cdot 10^{15}$ sites/cm². For a binary compound with a multitude of potential active sites, some of which may not even be able to bind H at all, the site density is even harder to estimate. Hence, we have used DFT calculations on the reconstructed surfaces of Ni₃P to calculate an upper bound of H binding sites. In practice, this is done by adding subsequent H-atoms to the calculated surface under unbound H₂(g) is preferred compared to the H-binding energy.

Table S3 Calculation of calculated unit cell surface area properties.

Bulk composition	Surface area (Å ²)	Surface layer	Orientation	Active sites/unit cell	Active sites/cm ²
Ni ₃ P	80.101	Ni ₄ P ₄	(0001)	7	8.74E+14
Ni ₃ P	80.101	Ni ₄ P ₄ +V _{Ni} +P	(0001)	5	6.24E+14
Ni ₃ P	80.101	Ni ₄ P ₄ +2P	(0001)	3	3.75E+14

As may be seen all the reconstructions has values from $4\text{--}9 \cdot 10^{14}$ sites/cm² compared to $\sim 2 \cdot 10^{15}$ sites/cm² as estimated by the average atom method (*vide infra*). Hence, using the above tabulated site densities would give a more accurate and higher TOF — but would still represent a lower limit estimate as clearly not all feasible sites are active at all overpotentials.

In the first method of TOF estimation we get the below:

ECSA is estimated for Ni₃P MP for three pristine samples after a short reductive induction period of -500mV vs RHE for 10min. Based on the estimated uncertainty for these surface area determinations the overall standard deviation is determined.

Figure S8 below shows a representative determination of scan rate dependence for the Ni₃P MP catalyst as well as for a Ni₅P₄ MP catalyst.

Ni₃P MP:

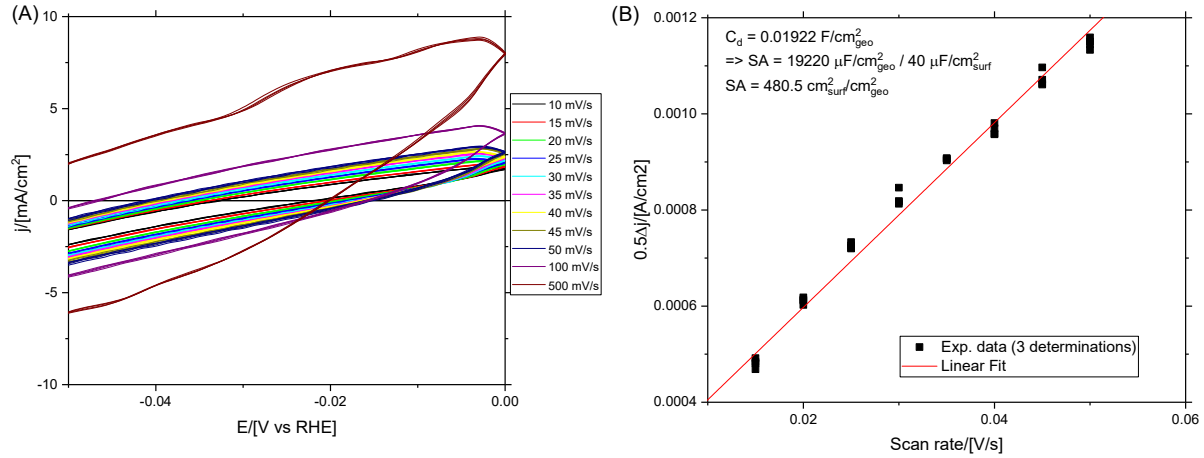


Figure S8 cyclic voltammetry measurement on Ni_3P MP in the non-Faradaic region nearest to the HER evolving potentials (A). (B) the ECSA estimation based on the capacitive current at -20mV vs RHE.

The other determinations gave 824.8 and 333.5 $\text{cm}^2_{\text{ECSA}}/\text{cm}^2_{\text{geo}}$ yielding an average of 546 ± 252 , a standard deviation of 36%.

For Ni_5P_4 MP and Pt foil catalyst the estimated ECSA surface areas were: 267 and 4.5 $\text{cm}^2_{\text{ECSA}}/\text{cm}^2_{\text{geo}}$, respectively.

Below are shown the ECSA determination for Ni_5P_4 MP catalyst using the same procedure as for Ni_3P MP catalyst:

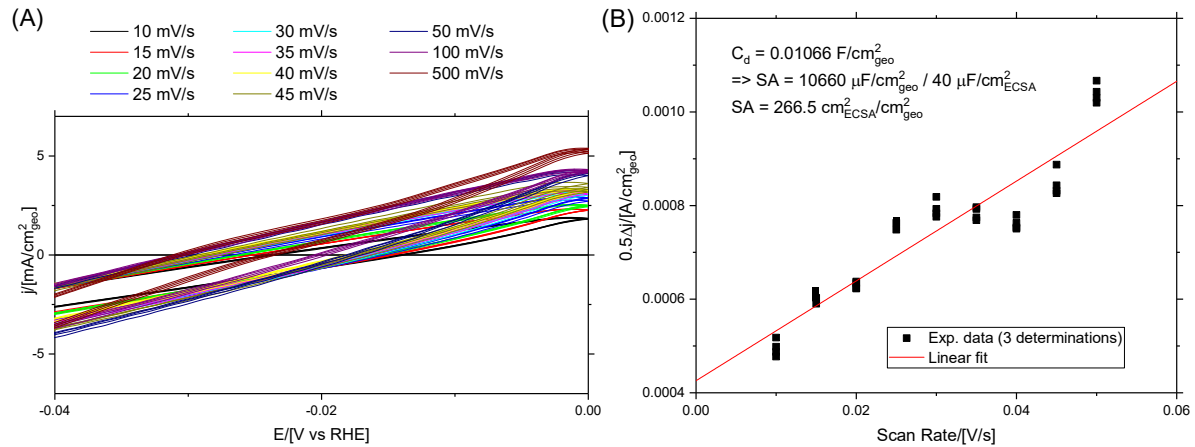


Figure S9 cyclic voltammetry measurement on Ni_5P_4 MPs in the non-Faradaic region nearest to the HER evolving potentials (A). (B) the ECSA estimation based on the capacitive current at -20mV vs RHE.

To convert the current to a H_2 flux:

$$\begin{aligned}
 H_2 \text{ flux} &= \frac{N_A}{1000 \cdot F \cdot n} \cdot \left| j \left[\frac{\text{mA}}{\text{cm}^2_{\text{geo}}} \right] \right| = \frac{6.022 \cdot 10^{23} \text{mol}^{-1}}{1000 \cdot \frac{96485.33 \text{C}}{\text{mol}} \cdot n} \cdot \left| j \left[\frac{\text{mA}}{\text{cm}^2_{\text{geo}}} \right] \right| \\
 &= 3.12 \cdot 10^{15} \frac{\text{H}_2}{\text{s}} \cdot \left| j \left[\frac{\text{mA}}{\text{cm}^2_{\text{geo}}} \right] \right|
 \end{aligned}$$

where n is number of electrons per H_2 molecule, N_A is Avogadro's constant, and F is Faraday's constant.

Estimating the average number of surface sites and the turnover frequency then becomes:

Ni_3P :

$$\begin{aligned}\# \text{ surface sites } Ni_3P &= \left(\frac{\text{atoms per unit cell}}{\text{unit cell volume}} \right)^{\frac{2}{3}} = \left(\frac{32}{351.65 \text{Å}^3} \right)^{\frac{2}{3}} = 0.202314 \text{Å}^2 \\ &= 2.02314 \cdot 10^{15} \text{ sites/cm}_{ECSA}^2\end{aligned}$$

$$\begin{aligned}TOF &= \frac{3.12 \cdot 10^{15} ((H_2/s)/cm_{geo}^2)/(mA/cm_{geo}^2)}{\# \text{ surface sites} \cdot A_{ECSA}} \cdot |j| \\ &= 2.82 \cdot 10^{-3} ((H_2/s)/\text{site})/(mA/cm_{geo}^2) \cdot |j|\end{aligned}$$

$$\begin{aligned}TOF_{\eta=100} &= 2.82514689 \cdot 10^{-3} ((H_2/s)/\text{site})/(mA/cm_{geo}^2) \cdot 26.6 \frac{mA}{cm_{geo}^2} \\ &= 0.075 H_2/s/\text{site}\end{aligned}$$

Ni_5P_4 :

$$\begin{aligned}\# \text{ surface sites } Ni_5P_4 &= \left(\frac{\text{atoms per unit cell}}{\text{unit cell volume}} \right)^{\frac{2}{3}} = \left(\frac{36}{438.51 \text{Å}^3} \right)^{\frac{2}{3}} = 0.18889 \text{Å}^2 \\ &= 1.8889 \cdot 10^{15} \text{ sites/cm}_{ECSA}^2\end{aligned}$$

$$\begin{aligned}TOF_{\eta=100} &= \frac{3.12 \cdot 10^{15} ((H_2/s)/cm_{geo}^2)/(mA/cm_{geo}^2)}{\# \text{ surface sites} \cdot A_{ECSA}} \cdot |j| \\ &= 6.1878 \cdot 10^{-3} ((H_2/s)/\text{site})/(mA/cm_{geo}^2) \cdot 79.6 \frac{mA}{cm_{geo}^2} = 0.49 H_2/s/\text{site}\end{aligned}$$

Pt :

$$\# \text{ surface sites } Pt (111) = \left(\frac{\text{atoms per unit cell}}{\text{unit cell volume}} \right)^{\frac{2}{3}} = 1.60 \cdot 10^{15} \text{ sites/cm}_{ECSA}^2$$

Surface sites density is $1.5 \cdot 10^{15}$ sites/cm² for Pt(111) single crystal²³ in reasonable agreement with the above estimation.

$$\begin{aligned}TOF_{\eta=100mV} &= \frac{3.12 \cdot 10^{15} ((H_2/s)/cm_{geo}^2)/(mA/cm_{geo}^2)}{\# \text{ surface sites} \cdot A_{ECSA}} \cdot |j| \\ &= 1.675 \cdot 10^{-1} ((H_2/s)/\text{site})/(mA/cm_{geo}^2) \cdot 71.81 \frac{mA}{cm_{geo}^2} = 9.74 H_2/s/\text{site}\end{aligned}$$

In the second estimate:

$$TOF_{\eta=100mV, Ni_3P} = 9.16 \cdot 10^{-3} ((H_2/s)/site)/(mA/cm_{geo}^2) \cdot 26.6 \frac{mA}{cm_{geo}^2} = 0.24 H_2/s/site$$

$$TOF_{\eta=100mV, Ni_5P_4} = 1.40 \cdot 10^{-2} ((H_2/s)/site)/(mA/cm_{geo}^2) \cdot 79.6 \frac{mA}{cm_{geo}^2} = 1.12 H_2/s/site$$

$$TOF_{\eta=100mV, Pt} = \frac{3.12 \cdot 10^{15} ((H_2/s)/cm_{geo}^2)/(mA/cm_{geo}^2)}{\#surface\ sites(1.5 \cdot 10^{15} sites/cm^2) \cdot A_{ECSA}} \cdot |j|$$

$$= 4.62 \cdot 10^{-1} ((H_2/s)/site)/(mA/cm_{geo}^2) \cdot 71.81 \frac{mA}{cm_{geo}^2} = 12.3 H_2/s/site$$

Below is the CV analysis corrected into TOF (A) using the first estimate (extreme upper estimate) of surface sites and (B) using the DFT based upper estimate of the number of surface sites.

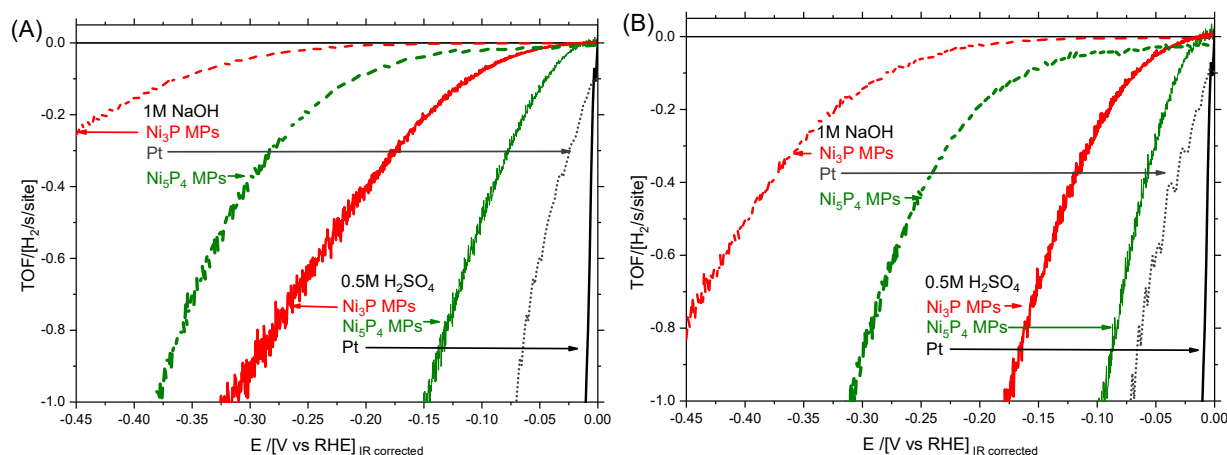


Figure S10 Turn-over frequency analysis on CV data for Ni_3P and Ni_5P_4 MPs in comparison to a Pt foil electrode. Potentials are shown versus RHE and corrected for solution resistance. (A) shows conservative estimate (based on crystal structure) and (B) estimate based on DFT determined upper limit of the number of active sites (yielding lower bound of TOF).

X-ray Photoelectron Spectroscopy:

XPS analysis was conducted on a Thermo K-Alpha spectrometer (monochromatic Al K_{α} source) without using a He flood gun for charge compensation. Since the electrodes contain significant C species calibration to adventitious C is impossible. Hence, the spectra were calibrated against Au by sputtering 5nm Au onto a representative catalyst surface. The Au lines at 83.96eV (for a monochromatic Al source) were referenced to the major carbon peak at 284.52eV. This carbon peak were used for all subsequent spectra to reference the binding energy axis.

To estimate the uncertainty of this method of calibration we use the second most intense C signal. Since, it has to be assumed that the carbon species do not depend on the catalyst (Ni_3P vs Ni_5P_4) nor are likely to be changed by electrocatalysis (graphite and the epoxy are inert, see below fabrication procedure), we use the secondary C peak to estimate the variation in the

calibration. The secondary carbon peak is on average at 286.08eV though for 6 samples of nickel phosphide catalysts (data not shown) the value varied from 285.99 to 286.17, hence the 90% confidence interval (by student t-test) is 0.19 or ± 0.2 eV. This is twice the common value of 0.1 eV generally observed by XPS and demonstrate the limit of assignment for this type of electrode.

Electrodes were fabricated by mixing 400mg catalyst, 40mg graphite, 52 mg Loctite Hysol 1C epoxy by mortar and pestle. The resulting paste was pressed in a 13mm die for 16 hours to partially cure (full cure takes 72 hours at room temperature). Subsequently the pellet was removed, the pellet fixed to Ti foil (using Ag-paint SPI chemicals) and the edges covered in Hysol 1C. After curing overnight at room temperature, the final electrode was heat cured at 120°C for 20min. The resulting electrode was polished by sanding paper starting from 200, 600, 1500 grit finalized with Al₂O₃ 5 μ m particle slurry. Finally, the electrode surface was masked with Teflon tape and a back contact made to a Cu wire (using adhesive Cu tape). The Cu wire was threaded through a glass tube and the contact sealed in acrylic hot melt (McMaster carr).

Prior to catalysis the electrode was sonicated in Milli-pore water to remove any polishing residue. Samples were reduced 30 min at -0.5V vs RHE in 0.5M H₂SO₄ then 10 CV cycles were recorded (from 0 to -0.5V vs RHE) to ensure full steady state performance of the electrode. The electrode was quickly removed from electrolyte, rinsed, dis-assembled, and dried under N₂ flow and stored under Ar in a glovebox until XPS analysis (transport to the XPS load-lock was done in a sealed contained under Ar). Wetting the back of the hot-melt with ethanol releases the hot-melt from the electrode and allows the electrode to be readily disassembled.

XPS analysis was performed on Ni₃P and Ni₅P₄ MP catalysts made into electrodes as described above.

For the pristine Ni₃P we observe three oxidation states of Ni in the Ni 2p region (Figure S11(A)) before catalysis from lowest to highest binding energy these are identified as nickel phosphide (Ni^{+δ} from Ni₃P), nickel oxide or hydroxide (Ni^{II}O/(OH)₂), and nickel phosphate ((Ni^{II})₃(PO₄)₂), respectively. Correspondingly, the P 2p region (Figure S11(B)) show only two discernable P oxidation states attributed to phosphide (P^{-δ}) and oxidized phosphorous, *i.e.* phosphate, phosphite, and/or hypophosphite (PO₄³⁻, PO₃³⁻, or PO₂²⁻). The same is observed for the pristine Ni₅P₄ MP catalysts (Figure S12(A) and (B)).

Post-catalytic turn-over on the Ni₃P MP catalyst, (Figure S11(C) and (D)) the oxidation states attributed to nickel phosphide (Ni^{+δ} and P^{-δ}) appears to shifts to lower binding energy; however, this shift is within the observed uncertainty. Nickel phosphides are well-known to oxidize upon air-exposure. It is therefore unsurprising that, what must be assumed to be the catalyst surface, is seen to consist mainly of highly oxidized phosphorous (PO₄³⁻) and multiple oxidized oxidation states of Ni. To interpret the multiple oxidation state of Ni, it is important to realize that XPS binding energies reflect the level of screening of core-electrons experience. As such, the Ni core-electron energies are sensitive to the anion's (oxide or phosphate) level of hydration, etc. Thus, the surface oxide is likely to consist of multiple species of differently hydrated phosphates and phosphites, and possibly nickel oxide. Oxidized nickel species (ascribed to Ni^{II}O/(OH)₂ in the pristine sample) in Ni₃P MP catalyst are observed to split into a higher binding energy peak (de-shielded/oxidized), likely the highly hydrated nickel oxide/phosphate, and a lower binding energy peak (shielded/reduced) nickel partial oxide/phosphate. Intuitively this makes sense, as the reduced catalyst is briefly air-exposed upon removal from the cell while still soaked in

electrolyte. As the reduced catalyst surface is oxidized an oxidation front would form and lead to a decreasing oxidation state with increasing depth from the particle surface. The brief exposure and presence of water could cause the formation of the highly oxidized phosphor-oxide but with a sharper transition to the reduced nickel phosphide. Whereas the as synthesized catalyst is air-exposed for a longer period of time and therefore is speculated to form a broader range of oxidation as a function of depth into the catalyst.

In contrast, the Ni_5P_4 MP catalyst shows only two oxidized states of Ni before and after catalysis although of different ratio. The low surface concentration of nickel phosphide in the hybrid-electrode (<1% Ni and P, respectively) makes the accurate quantification of Ni and P species in the various chemical states (nickel phosphide and phosphor-oxide) impossible. The relative ratio of Ni in nickel phosphide compared to surface nickel phosphor-oxide is strongly dependent on the exact time of air-exposure during cleaning, electrode deconstruction, and transfer from reaction cell to glovebox for storage and from there to the XPS load-lock. Due to this we expect a poor reproducibility of this air-exposure, making it unlikely that the relative ratio of nickel phosphide to nickel phosphor-oxide is an indication of the inherent susceptibility of the catalysts to corrosion/oxidation.

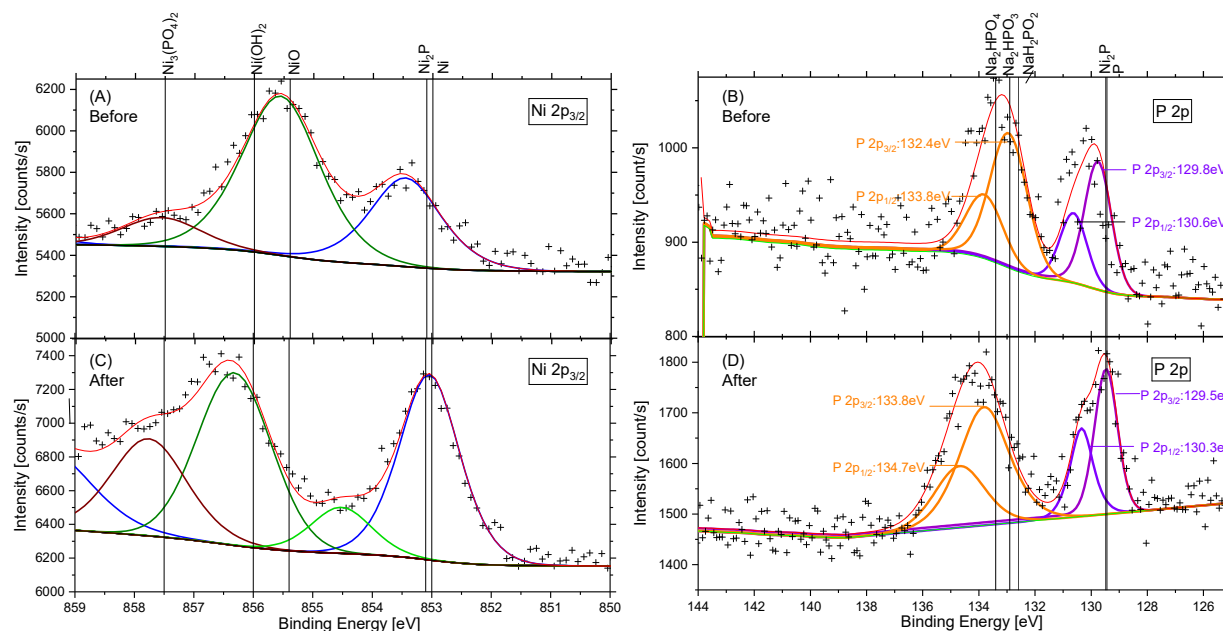


Figure S11 XPS analysis of Ni $2p_{3/2}$ region (A&C) and P $2p$ region before and after catalytic turn-over (B&D) on Ni_3P MP catalysts.

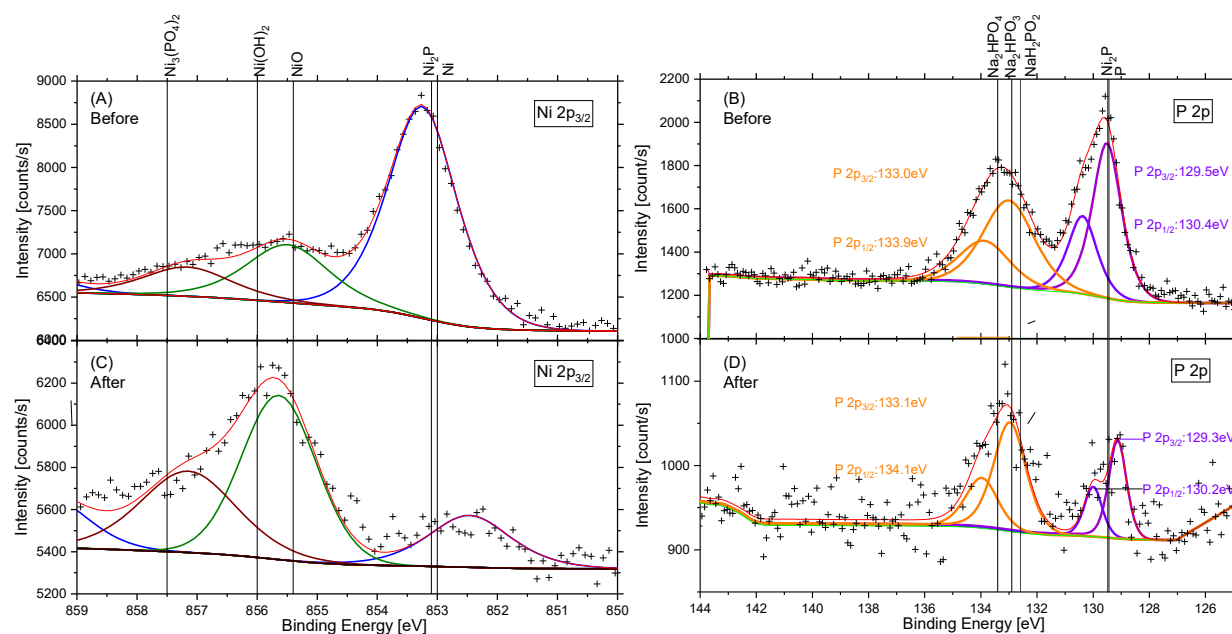
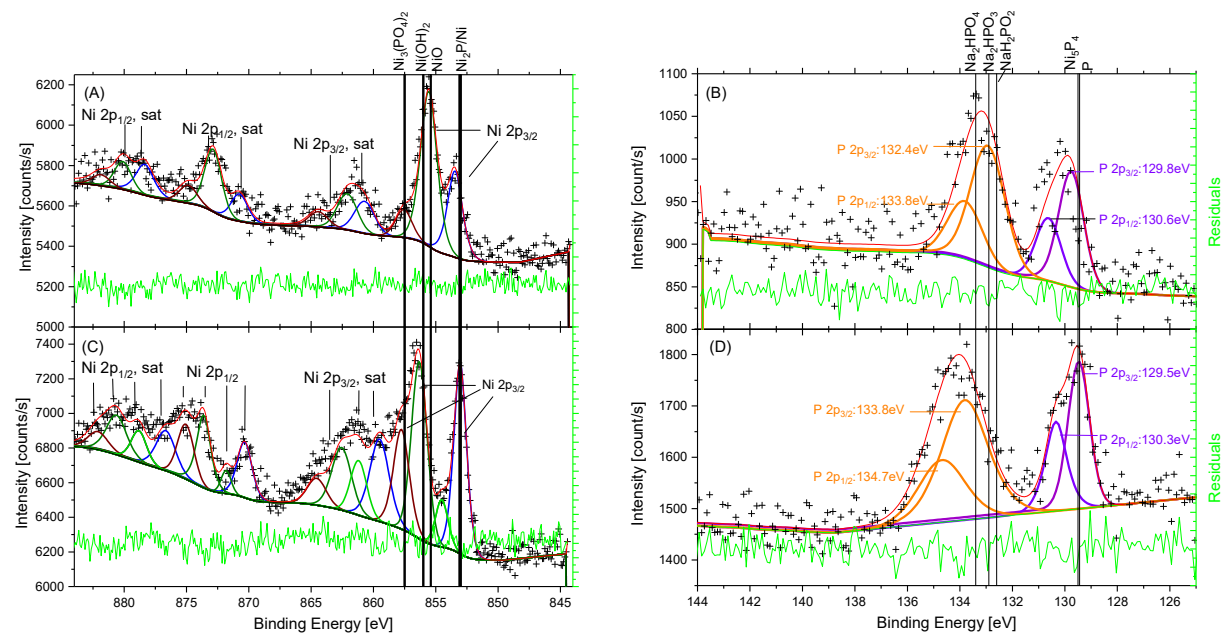


Figure S12 XPS analysis of Ni 2p_{3/2} region (A&C) and P 2p region before and after catalytic turn-over (B&D) on Ni₅P₄ MP catalysts.



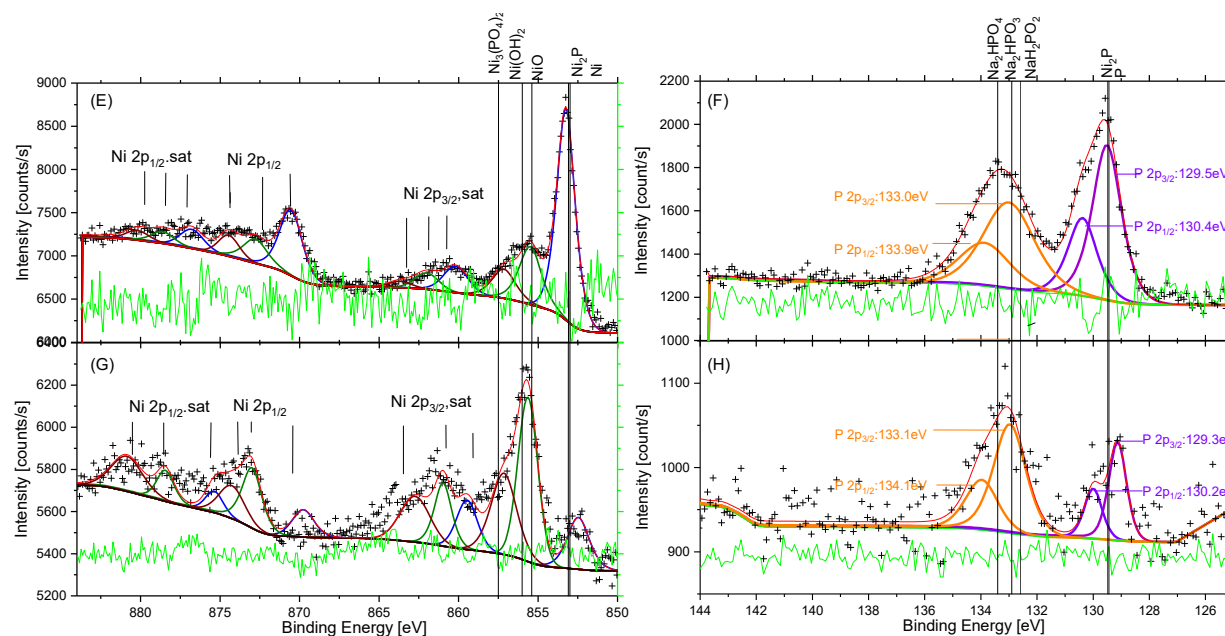


Figure S13 XPS analysis of Ni 2p region (A&C) and P 2p region before and after catalytic turn-over (B&D) on Ni_3P MP catalysts. XPS analysis of Ni 2p region (E&G) and P 2p region before and after catalytic turn-over (F&H) on Ni_5P_4 MP catalysts. In light green is shown the residual function, the absence of peak in this trace confirms the complete fits of the spectra.

To verify that the surface of the catalyst is not containing any impurities we performed a survey scan (see Figure S2Figure S14) of the Ni_3P MP catalyst post catalysis. We observe, Ni, P, C, O, S, N, Mg, and Si, the first four elements are due to the catalyst and graphite/epoxy electrode. S and N is due to the sulfuric acid electrolyte and ammonium adsorbed in electrolyte from ambient air exposure. Mg and Si is from Talc which is an additive in the Hysol 1C epoxy. Hence, there are no additional elements not arising from the electrode or electrolyte and the presence of impurities can be disregarded.

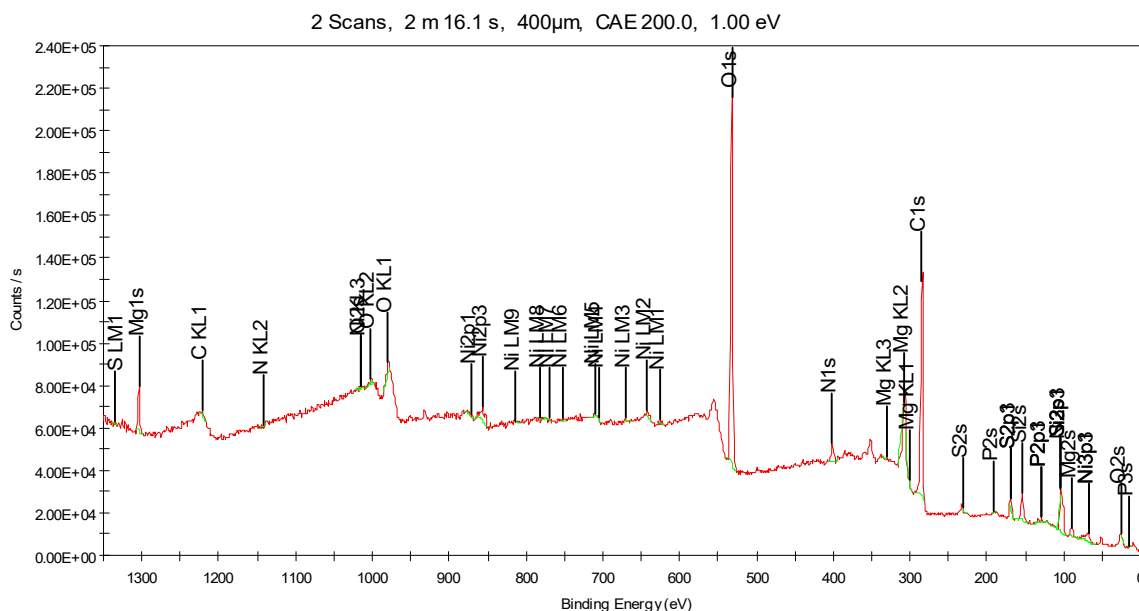


Figure S14 XPS survey analysis after catalysis 30 min. in 0.5M H₂SO₄.

KSCN poisoning experiments:

KSCN has been used in literature to selectively poison metal sites of HER catalysts.²⁴ These authors showed that in the case of HER catalysis from Ru on C₂N support, they could discriminate between C-N and Ni contributions to HER (both are known to be active for HER independently) by selective poisoning of the Ru sites which binds SCN⁻. Here, we use this method to selectively poison the nickel sites but leaving the P sites active for HER.

Using this procedure, we first demonstrated the adsorption of SCN⁻ on pure nickel and on nickel phosphide. We add KSCN to a catalyst suspension at approximately 4% of the total number of surface atoms, based on the upper limit of the number of surface sites (determined previously by ECSA, see SI). Free SCN⁻ adsorption in solution was detected by UV/Vis spectroscopy at 216 nm.

Since the ECSA for Ni₃P MP electrodes are 546 cm²_{ECSA}/cm²_{GEO} and the upper limit of number of surface sites is 2.02 · 10¹⁵ atoms/cm² (see TOF calculations above). Our electrodes use 50mg catalyst pressed in a 6mm diameter die (0.28 cm²_{GEO}), which means that 1 equivalent of surface sites would be:

To ensure significant adsorption of KSCN, 50mg catalyst powder is mixed with 400 µL 0.00005 M KSCN (0.2 · 10⁻⁷ mol) or 4% of the upper limit of surface sites. This suspension is sonicated 1 hour and left to equilibrate at room temperature. UV/Vis spectra of the mother liquid are recorded to quantify the amount of SCN⁻ that is removed. Adsorption is measured for Ni₃P and Ni₅P₄ MP catalyst powder as well as a pure Ni powder (Sigma <150µm).

Figure S15 below shows the absorption spectrum for standard solutions of KSCN in water. A spectral feature is observed at 216nm that is proportional to the concentration of KSCN. Using

Lambert-Beers law for absorption we can correlate this peak intensity to the concentration of KSCN.

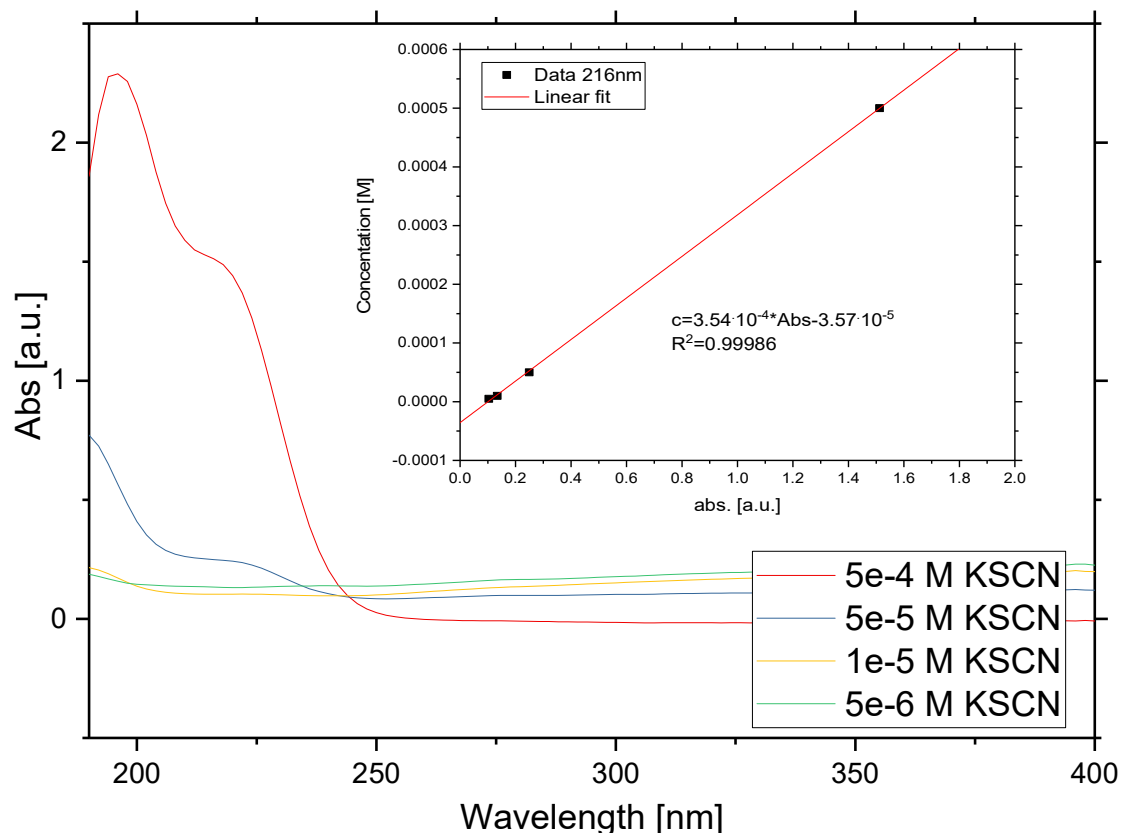


Figure S15 UV/Vis spectra of KSCN standard solutions and Lambert-Beer's law calibration curve at 216nm (insert).

Post-adsorption only the mother liquid of the Ni MP sample is colored a clear green color (~394nm) as is clearly observed in the absorption spectra in Figure S16 below.

The table below shows the calculated concentration of SCN^- in the mother liquid before and after adsorption. *After allowing for equilibration, the mother liquid show that significant amounts SCN^- is absorbed onto Ni_3P (43%) whereas the Ni_5P_4 show near complete SCN^- adsorption (96%) — opposite to what might be expected based on the Ni/P ratio in the bulk catalysts. We attribute this difference in the number of SCN^- -accessible Ni sites in the two catalysts to the difference in surface Ni sites available in the reconstructions versus in the bulk.*

Table S4 KSCN adsorption results measured by UV/Vis absorption.

Catalyst	Measured adsorption [a.u.]	Calculated concentration [μM]	Percent SCN^- adsorbed [%]
Blank	0.2316	56.8	0
Ni	0.0985	-0.8	101
Ni_3P MP	0.1923	32.4	43
Ni_5P_4 MP	0.1068	2.1	96

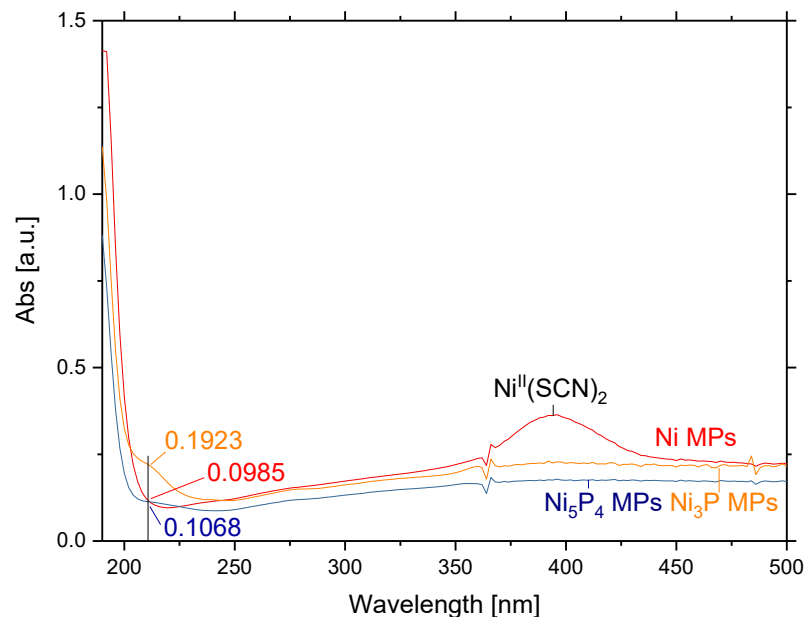


Figure S16 UV/Vis spectrum of the mother liquid of Ni, Ni₃P, and Ni₅P₄ powders post 65 hours adsorption.

To test the effect SCN⁻ poisoning on catalysis we estimate the number of surface sites in the catalyst using the ECSA estimation of the upper bound of the number of surface sites. Figure S17 shows the CP analysis (-10mA/cm²_{geo}) as two equivalents of KSCN are added to the catalyst poisoning the Ni-sites.

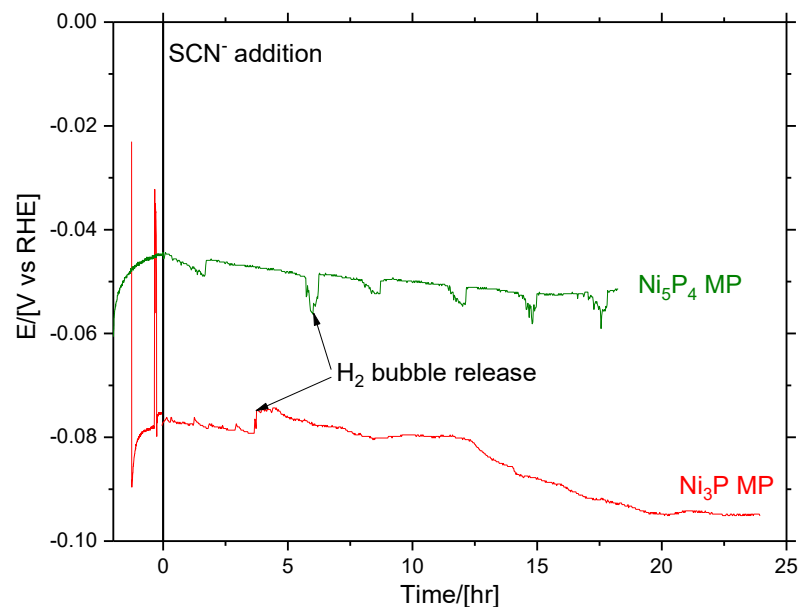


Figure S17 CP analysis at -10mA/cm² of Ni₃P and Ni₅P₄ MP catalysts the with addition of metal site poison SCN⁻ at Time = 0. Catalyst induction period is seen at negative times.

For the Ni₃P MP catalyst the addition of SCN⁻ is followed by an ~13 hr induction period where no change in the potential required for -10mA/cm² is observed after which the potential drops

rapidly. Conversely for the Ni_5P_4 MP catalyst the potential is almost immediately affected. After 18 hr the potential has increased 17 and 7mV for the Ni_3P and Ni_5P_4 MP catalyst, respectively.

Since our analysis of the surface reconstructions showed that various surface sites were active at different potentials we investigate the effect of the poisoning on the rate determining step rather than the absolute value of the potential at an arbitrary current density. From the Tafel analysis (current change per unit potential change in the region not limited by mass transport) of Ni_3P and Ni_5P_4 before and after Ni-site poisoning the Tafel slope is unchanged within the experimental error. The Tafel slope is unaffected (black trace before poisoning and red trace after poisoning), within the experimental uncertainty. The exchange current density for Ni_3P appears to be reduced but the effect is minor and within the noise. These results show that SCN-poisoned Ni sites do not contribute to the catalytic current. By deduction, the remaining surface sites, e.g. P sites, are implicated as the catalytic sites for HER. Figure 4 in the main text show that per our DFT calculation the bulk termination of the $\text{Ni}_3\text{P}(001)$ only show Ni centered binding whereas only the $\text{Ni}_3\text{P-Ni}_4\text{P}_4+\text{V}_{\text{Ni}}+\text{P}$ reconstruction show H-binding sites on P.

While it is clear that this DFT prediction is not experimental verification that the (001) facet is the majority exposed facet, it gives theoretical evidence identifying P as the active site on reconstructed Ni_3P and Ni_5P_4 .

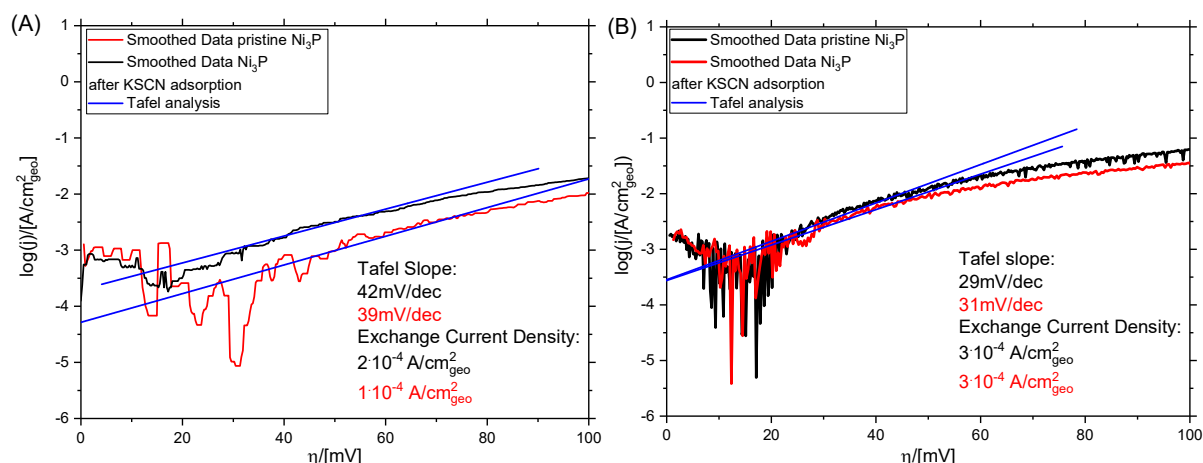


Figure S18 (A) Tafel analysis of Ni_3P MP catalyst before (black) and after (red) KSCN addition and adsorption. (B) Ni_5P_4 MP catalyst before (black) and after (red) KSCN addition and adsorption.

DFT calculation details:

Bulk lattice constants

Table S5 Bulk computed and experimental lattice constants and crystallographic angles. Excellent agreement is found between the computed and experimental values, the latter of which are enclosed in parenthesis. Lattice constants are in Å.

Bulk composition	<i>A</i>	<i>b</i>	<i>c</i>	α	β	γ
Ni		3.4998 (3.5276)				90 (90)
Ni_3P	8.9221 (8.9499)		4.3626 (4.3850)			90 (90)
Ni_5P_2	6.5511 (6.5795)		12.220 (12.261)	90 (90)		120 (120)

Bulk and surface phase diagram

At equilibrium, the free energy of forming a phase from its constituent elements is given by

$$\Delta G = \sum_{i=1}^{n_{typ}} \mu_i \quad (\text{Equation S1})$$

where μ is the chemical potential and i is an index that runs from 1 to the number of types of atoms, n_{typ} . Specifying ΔG for Ni(fcc), Ni₃P, and Ni₅P₂ we obtain

$$\Delta G(\text{Ni}) = \mu_{\text{Ni}} \quad (\text{Equation S2a})$$

$$\Delta G(\text{Ni}_3\text{P}) = 3\mu_{\text{Ni}} + \mu_{\text{P}} \quad (\text{Equation S2b})$$

$$\Delta G(\text{Ni}_5\text{P}_2) = 5\mu_{\text{Ni}} + 2\mu_{\text{P}} \quad (\text{Equation S2c})$$

Solving Equations S2b and S2c for μ_{Ni} gives the phase boundary between Ni(fcc) and Ni₃P

$$\mu_{\text{Ni}} = 2\Delta G(\text{Ni}_3\text{P}) - \Delta G(\text{Ni}_5\text{P}_2) \quad (\text{Equation S3})$$

At constant T (0 K) and P, we can replace ΔG with ΔE^{DFT} , which gives $\mu_{\text{Ni}} = -0.34$ eV as the chemical potential of Ni at the phase boundary between Ni₃P and Ni₅P₂. We choose Ni₅P₂ because it is the second most Ni-rich Ni_xP_y compared to Ni₃P. Similarly, we can find that $\mu_{\text{Ni}} = 0$ eV at the phase boundary between Ni(fcc) and Ni₃P. Therefore, Ni₃P is the most stable bulk phase of Ni_xP_y between $\mu_{\text{Ni}} = 0$ and -0.34 eV.

The bulk phase diagram provides a window of μ_{Ni} where we investigate the stability of Ni₃P(001) bulk-derived and reconstructed surfaces. The surface free energy is calculated in different chemical environments using the following equation, which is found elsewhere.^{17,25}

$$\Omega = \frac{1}{A} (\phi + \Gamma_{\text{Ni}} \Delta \mu_{\text{Ni}}) \quad (\text{Equation S4})$$

Here, A is the surface area, $\Delta \mu_{\text{Ni}}$ is the chemical potential of Ni referenced to Ni(fcc) at 0 K, and ϕ and Γ are

$$\phi = E_{\text{slab}}^{\text{DFT}} - N_{\text{P}} E_{\text{Ni}_3\text{P}}^{\text{DFT}} + \Gamma_{\text{Ni}} \Delta \mu_{\text{Ni}} \quad (\text{Equation S5a})$$

$$\Gamma_{\text{Ni}} = 3N_{\text{P}} - N_{\text{Ni}} \quad (\text{Equation S5b})$$

where E_{slab} is the DFT total energy of the slab model described in the computational methods section, $E_{\text{Ni}_3\text{P}}$ is the DFT total energy of bulk Ni₃P, and N_{Ni} and N_{P} are the total number of Ni and P atoms in the slab model.

Bulk Ni₃P has two distinct layer compositions along the *c* crystallographic axis, Ni₈ and Ni₄P₄. Surface cleavage along (001) could therefore produce two different bulk-derived

terminations. We investigate the stability of these bulk-derived terminations compared to surface reconstruction including the formation of Ni and P adlayers and vacancies. Figure S19(a) shows the free energy of various structures tested in this investigation and the structures of the most stable candidates.

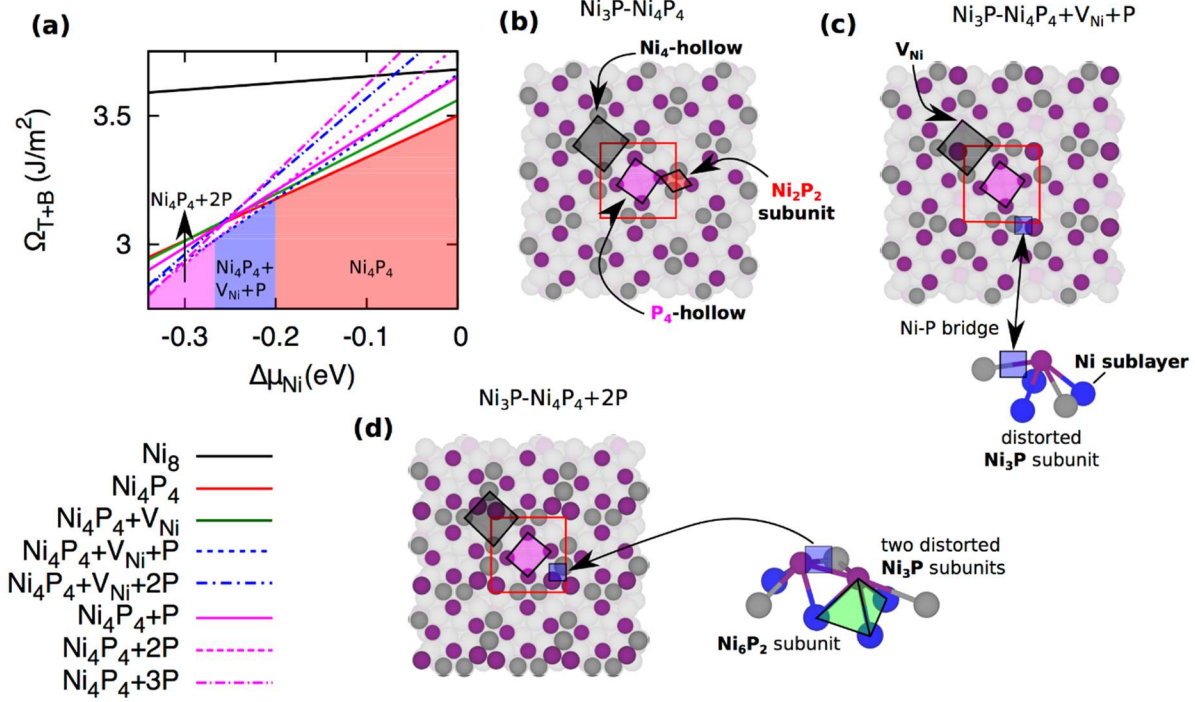


Figure S19 DFT stability analysis of $\text{Ni}_3\text{P}(001)$ bulk-derived and reconstructed surfaces. (a) Combined top and bottom surface free energies as function of the Ni chemical potential. Surface structural models of the (b) bulk-derived $\text{Ni}_3\text{P-Ni}_4\text{P}_4$, and reconstructed (c) $\text{Ni}_3\text{P-Ni}_4\text{P}_4+\text{V}_{\text{Ni}}+\text{P}$ and (d) $\text{Ni}_3\text{P-Ni}_4\text{P}_4+2\text{P}$ terminations. Regions of Ni chemical potential where different surface phases are stable are shaded. Labels and structural insets highlight important structural features on the surface. Blue Ni atoms in insets correspond to sublayer Ni.

First off, $\text{Ni}_3\text{P-Ni}_4\text{P}_4$ (see Figure S19a, red line) is far more stable than $\text{Ni}_3\text{P-Ni}_8$ (black line) in comparing the bulk-derived terminations. The surface possesses repeating Ni_2P_2 subunits, which form Ni_4 and P_4 -hollows with their edges (see Figure S19b). $\text{Ni}_3\text{P-Ni}_4\text{P}_4$ can be stabilized at $\mu_{\text{Ni}} < -0.2$ eV by the formation of a Ni vacancy (see Figure S19c), creating an incomplete Ni_2P_2 subunit and Ni_4 -hollow (right triangle), and deposition of a P adatom, which forms between two Ni_2P_2 subunits and creates a distorted Ni_3P subunit with a Ni_3 -hollow in the sublayer to generate $\text{Ni}_3\text{P-Ni}_4\text{P}_4+\text{V}_{\text{Ni}}+\text{P}$ (see Figure S19a, blue dash-dot line). This highlights that the sublayer plays an important role in binding adlayer P species. The adsorption of an additional P adatoms to form $\text{Ni}_3\text{P-Ni}_4\text{P}_4+\text{V}_{\text{Ni}}+n\text{P}$ where $n > 1$ is unfavorable. Instead, at μ_{Ni} lower than -0.27 eV, the surface prefers $\text{Ni}_3\text{P-Ni}_4\text{P}_4+2\text{P}$, which has complete Ni_2P_2 subunits connected by two adlayer P atoms along the a crystallographic direction. Further adsorption of P is only stable at μ_{Ni} values where bulk Ni_5P_2 is preferred to Ni_3P . The fact that $\text{Ni}_3\text{P}(001)$ forms P-enriched surface reconstructions is striking considering the bulk composition is so Ni-

rich. This analysis therefore highlights that even under the most Ni-rich conditions, P stabilizes the surface by passivating the dangling Ni bonds.

Table S6 Calculated binding energies:

n _H	Ni ₄ P ₄	Ni ₄ P ₄ +V _{Ni} +P	Ni ₄ P ₄ +2P
1	-0.5298480154	-0.2895636223	-0.0819090175
2	-0.5046536603	-0.09223079266	0.1176333125
3	-0.1472252408	0.03839020826	
4	-0.1660777393	0.1272880539	
5	0.1048585423		
6	0.1165746757		

Table S7 Calculated electron density:

Sites	s e-	p e-	d e-	Charge	# in unit cell
Ni1	0.7538	5.9840	8.7307	0.5315	4
Ni2	0.7521	5.9839	8.7304	0.5336	4
Ni3	0.6506	5.9787	8.6713	0.6994	4
Ni4	0.6502	5.9788	8.6725	0.6985	4
Ni5	0.6969	5.9802	8.6978	0.6251	4
Ni6	0.6967	5.9801	8.6976	0.6256	4
P1	1.4639	3.2991	1.5036	-1.2666	4
P2	1.4618	3.3003	1.5124	-1.2745	4

Projected Density Of States (PDOS)

PDOS for Ni₃P:

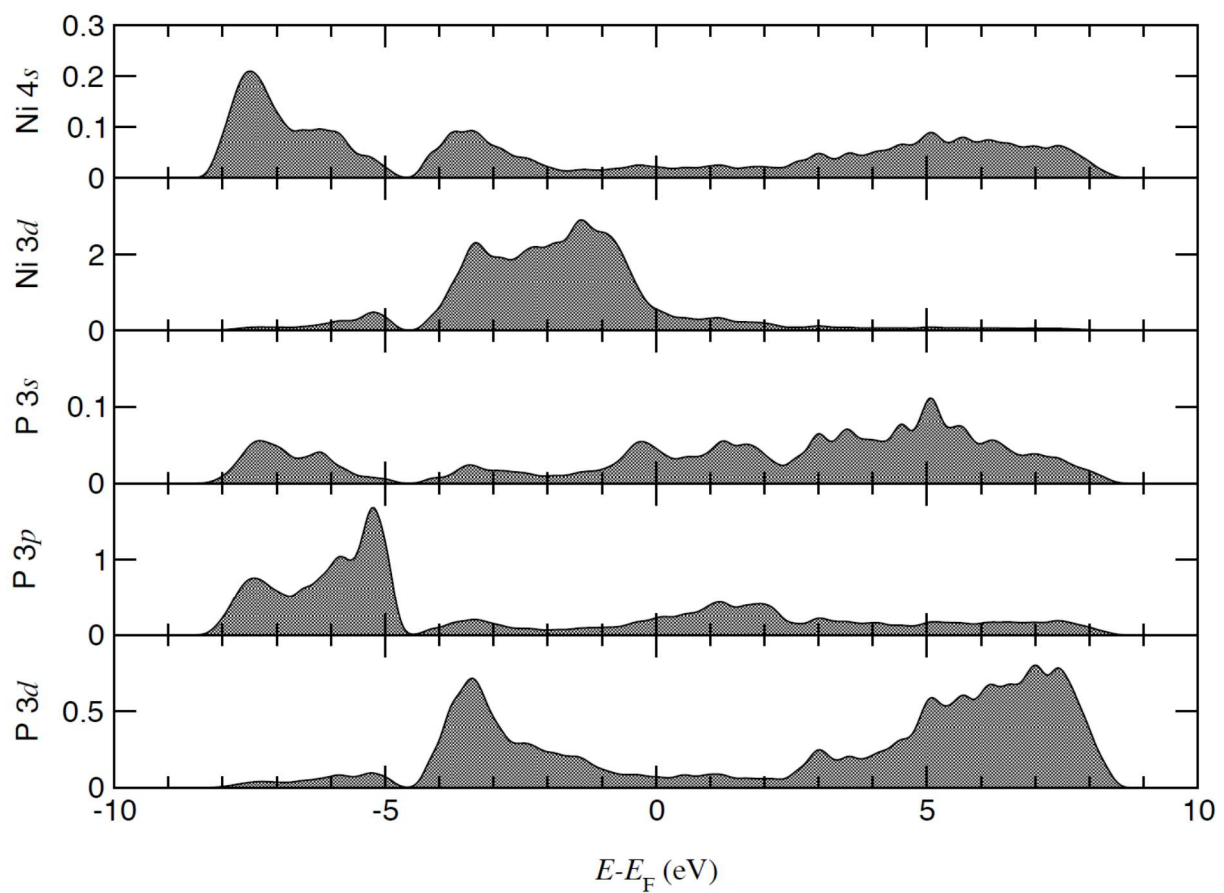


Figure S20 PDOS averaged over all atoms in the unit cell.

Charge Density for Ni_3P bulk structure along the $\text{Ni}_3\text{P}(001)$ direction and bulk- Ni_4P_4 termination.

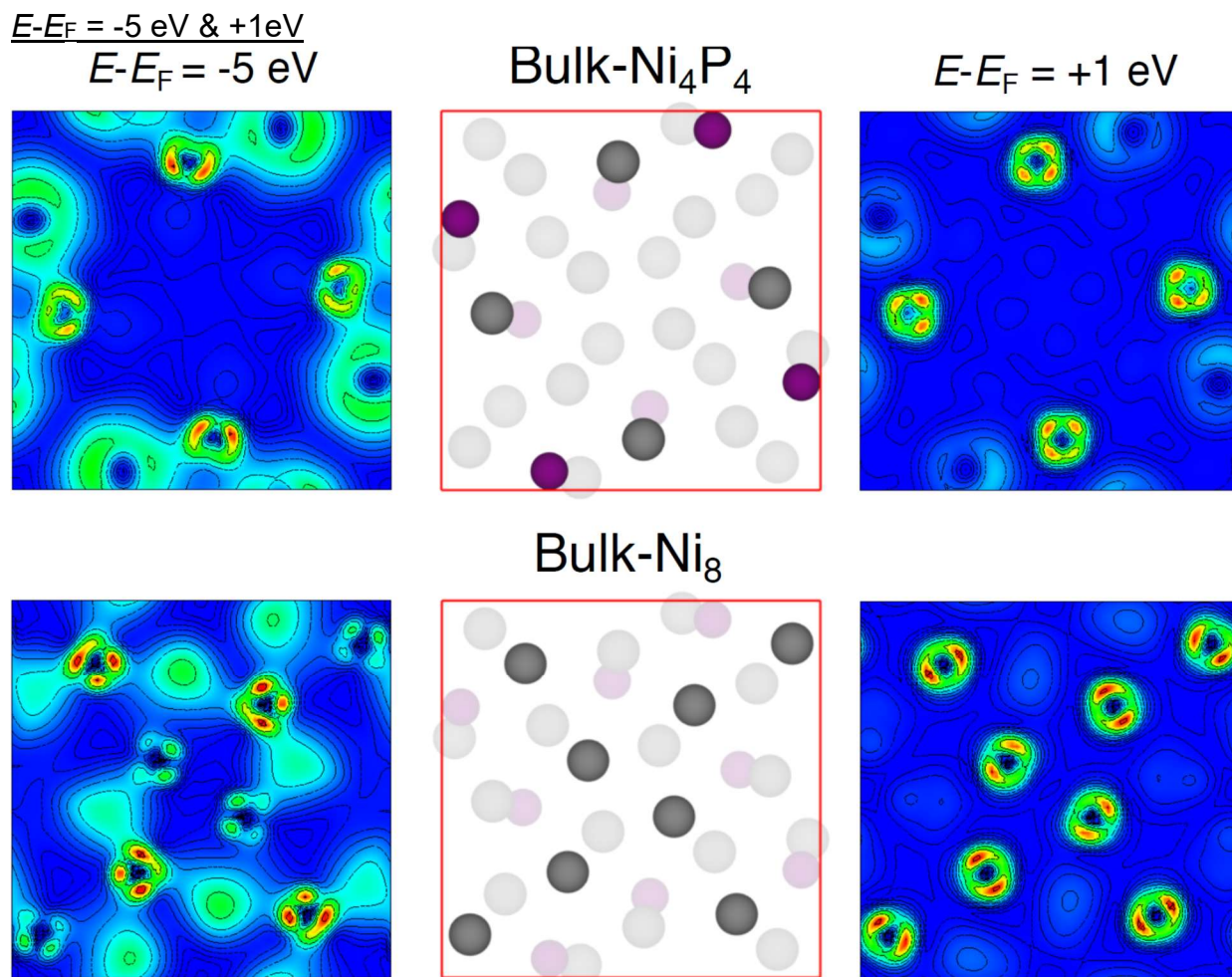


Figure S21 local PDOS between $E-E_F = -5$ and -4.9 eV for each layer of Ni₃P, Ni₂P, and Ni₅P₄ (left), Structure (center), and local DOS between $E-E_F = +1$ and 1.1 eV (right)

These plots show the integrated local PDOS. Red/blue regions denote higher/lower (50/1% the maximum) electron density and dotted lines show order of magnitude changes in the electron density. The DOS states plots on the left show that there is a peak for both the Ni 3d and P 3p orbitals at $E-E_F = -5$ eV. Most layers, with the exception of Ni₂P-Ni₃P, show Ni 3d-P 3p hybridization, *i.e.* Ni-P bonding orbitals.

For The maximum values here are not necessarily the same as above; therefore, we cannot make intensity comparisons. The DOS states plots above show that there is energy overlap of the Ni 3d and P 3p orbitals at $E-E_F = +1$ eV. All layers show localized states on Ni and P suggesting that these unfilled states are anti-bonding Ni-P orbitals.

Surface area measurements:

N₂ adsorption measurements at 77 K were performed to evaluate the surface area of the materials. The measurements were conducted with a Micromeritics 3Flex adsorption analyzer. For each measurement, $\sim 0.5 - 1$ g of sample was activated at 120 °C under

dynamic vacuum prior to adsorption. N₂ of ultra-high purity (99.999%) was used as the feed gas and liquid nitrogen was used as the coolant to maintain the sample at cryogenic temperature.